Alternating pattern formation in oscillatory media with spatially uniform and nonuniform global feedback

Zhilin Qu [1,*] Chunli Huang [2] and Fengze Sui [3]

[1] *Department of Medicine (Cardiology) and Department of Computational Medicine, David Geffen School of Medicine at UCLA, University of California, Los Angeles, California 90095, USA*

[2] *School of Mathematics and Statistics, Guangdong University of Foreign Studies, Guangzhou 510420, China*

[3] *School of Computer Science and Technology, Harbin Institute of Technology, Shenzhen 518055, China*

(Received 10 January 2026; accepted 14 May 2026; published 14 July 2026)

Alternating (temporally period-2) stripes, clusters, and labyrinths have been observed in chemical and biochemical reactions, in Min-protein dynamics in *E. coli* and *in vitro* systems, and in calcium alternans in cardiac myocytes. However, the mechanisms underlying the formation of these spatiotemporal patterns and the transitions among them remain incompletely understood. In this article, we use an amplitude-equation (AE) approach to perform theoretical analysis and numerical simulations to elucidate the mechanisms of the alternating pattern formation and selection, and we then use reaction-diffusion models to validate the predictions of the AE model. It was shown previously that in chemical reactions and cardiac myocytes, a global feedback loop plays a key role in the formation of alternating clusters. Based on previous AE models developed to describe cardiac alternans dynamics, we first develop an AE model that incorporates either a spatially uniform global feedback (UGF) loop or a spatially nonuniform global feedback (NUGF) loop. The NUGF is represented by a spatially Gaussian-weighted function. We then use the AE model to conduct nonlinear stability analysis to reveal the mechanisms underlying the emergence of alternating patterns under different feedback conditions. Under positive UGF, no patterns can form. When the UGF is negative, the stable patterns are only multiple stripes and circular clusters. For stripe patterns, they may be spatially periodic or random as long as they satisfy the requirements for pattern selection. For circular clusters, a medium can support one or multiple circular alternating clusters of the same radius depending on the size of the medium. Under NUGF, in addition to stripe and circular-cluster patterns, lateral instability arises when the width of the Gaussian function falls within an intermediate range, leading to transitions from stripes or circular clusters to labyrinths. Other initial-condition-dependent patterns are also observed under NUGF. Under UGF, the width of the stripe can be periodic or random, but under NUGF, the patterns become less random in space as the feedback strength increases. Finally, we incorporate the UGF and NUGF loops into several reaction-diffusion models, including the Belousov-Zhabotinsky reaction model, the carbon monoxide oxidation model, and the periodically paced FitzHugh-Nagumo model. These models successfully reproduce the alternating pattern dynamics predicted by the AE model, validating the theoretical predictions.

DOI: 10.1103/r3d8-2p3x

I. INTRODUCTION

Pattern formation is a fundamental process in natural and engineered systems [1,2]. In chemical and biological systems, Turing instability [3–7] is a widely known mechanism for formation of steady-state patterns including stripes, spots, and labyrinths. Turing instability is promoted by a faster diffusion of the inhibitor than that of the activator in a reaction-diffusion system [3]. In oscillatory media (or periodically paced excitable media), oscillatory patterns or more complex spatiotemporal patterns have been widely demonstrated [7,8]. Oscillatory Turing patterns have been shown in reaction-diffusion systems when Turing bifurcation and Hopf bifurcation coexist [9–11], in which oscillations superimpose on the Turing patterns. Another type of widely observed oscillatory patterns that are different from the patterns from Turing-Hopf bifurcations are alternating (period-2) clusters or clustered standing waves in oscillatory media [12–18]. One set of experiments are chemical reactions with a global feedback loop [12–14], in which alternating stripes [Fig. 1(a)] or clusters [Fig. 1(b)] occur. These alternating patterns are temporally period-2 and spatially antiphase in neighboring regions [see the line scan in Fig. 1(a)].

An example of this type of pattern in biological systems is subcellular calcium alternans in periodically paced cardiac myocytes [19–24], which exhibit spatially out-of-phase alternating patterns [Fig. 1(c)], similar to the alternating stripes in the chemical reactions shown in Fig. 1(a). Alternans is a widely observed phenomenon in cardiac systems that is linked to arrhythmias and sudden death [19,25,26].

*Contact author: zqu@mednet.ucla.edu

Published by the American Physical Society under the terms of the Creative Commons Attribution 4.0 International license. Further distribution of this work must maintain attribution to the author(s) and the published article's title, journal citation, and DOI.

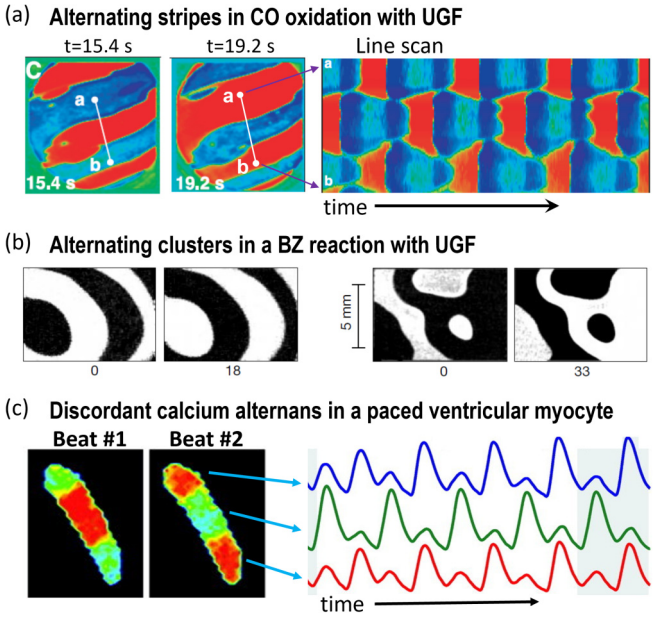


FIG. 1. Alternating clusters in chemical reactions with UGF and cardiac myocytes. (a) Alternating stripes in catalytic CO oxidation on a platinum with a UGF, modified from Kim *et al*. [14]. The left two panels are snapshots of opposite phases (at 15.4 and 19.2 s) and the right panel is a line scan (space-time plot) from the marked line [from (a) to (b)]. (b) Alternating clusters in BZ reaction [12]. (c) Discordant calcium alternans in a mouse ventricular myocyte [22]. The right panels are calcium snapshots for two consecutive beats, and the left panel shows recordings of calcium from three locations as marked.

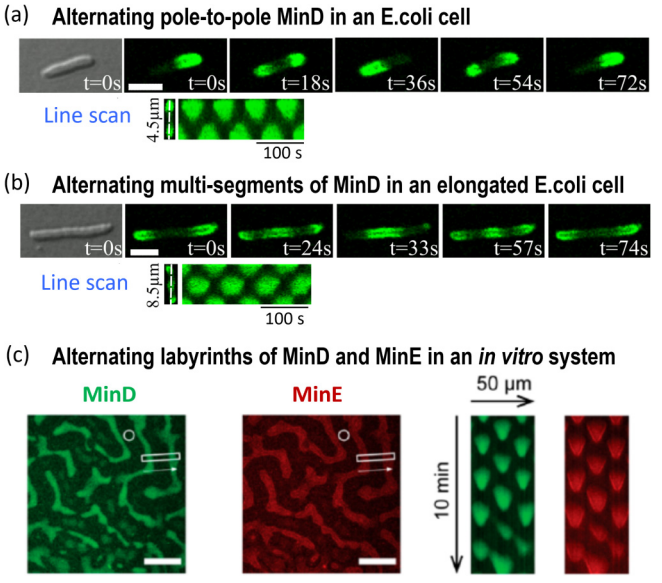


FIG. 2. Alternating patterns in *E. coli* and Min-protein systems. (a) Alternating segments of MinD in *E. Coli*, modified from Bonny et al [35]. Upper panels: Pole to pole oscillations of MinD in a normal *E. coli* cell. (b) Lower panels: Oscillating clusters of MinD in an elongated *E. Coli* cell. (c) Alternating labyrinths of bacterial proteins from experiments of an *in vitro* system of MinD and MinE, modified from Kretschmer *et al*. [17]. Left two panels are snapshots of MinD and MinE. Right two panels are line scans from the corresponding regions marked by the open bars on the left panels.

Another widely known example of this type of pattern in biological systems is an alternating standing-wave pattern of Min proteins in *Escherichia coli* (*E. coli*) [27–38] [Figs. 2(a) and 2(b)]. The pole-to-pole oscillation of the Min proteins ensures the division of *E. coli* in the middle and thus the fidelity of cell division. Furthermore, in elongated cells (or when cell division is blocked [34]), multiple segment patterns of Min proteins can form [Fig. 2(b)] [35,36,38]. These patterns agree with the one seen in chemical reactions with global feedback or in cardiac myocytes. An interesting observation is that in an *in vitro* system of Min proteins, alternating labyrinth patterns are observed [Fig. 2(c)] [17]. Alternating labyrinth patterns are also observed in Belousov-Zhabotinsky (BZ) reactions [18].

Computer simulations [39–42] and theoretical studies [43,44] have shown that the formation of alternating patterns can be caused by a global feedback loop, agreeing with the chemical reaction and cardiac myocyte experiments. While computer simulations have shown the segment patterns in the *E. coli* cell models [30–33,35], no modeling studies have been carried out to show alternating labyrinth patterns. Furthermore, the general mechanisms for the formation of the alternating stripes and particularly the mechanisms for the transition from alternating stripe patterns to alternating labyrinth patterns are unknown. In a recent Letter [45], we showed that the transition from alternating stripes to alternating labyrinths can occur when the spatially uniform global feedback (UGF) [Fig. 3(a)] becomes a spatially Gaussian-weighted global feedback or spatially nonuniform global feedback (NUGF) [Fig. 3(b)]. We first showed this in a computer simulation of a BZ reaction model with NUGF and then used an amplitude equation (AE) approach to perform stability analyses to reveal the underlying dynamical instability leading to the formation of labyrinth patterns. In this study, we extend the AE approach with the presence of UGF and NUGF to perform theoretical analyses on pattern formation and pattern dynamics. Computer simulations with mathematical models of different biological or biochemical media are used to validate the theoretical predictions from the AE model. More specifically, we first perform theoretical analysis of the AE model under UGF to predict instabilities leading to different patterns in one-dimensional (1D) and two-dimensional (2D) media. This provides a theoretical basis for the alternating clusters observed in chemical reaction experiments and computer simulations [12–14] as well as subcellular calcium alternans in cardiac myocytes [19–24]. We then extend our recent Letter published in this journal [45] in which a Gaussian-weighted global feedback loop was used to investigate the formation of alternating labyrinths observed in Min protein systems [17] and chemical reactions [18]. We extend the results by performing a more detailed stability analysis and new patterns in the models, providing a more complete view of alternating pattern dynamics in oscillatory media.

The results are presented in Sec. II, which is organized as follows. Section II A is for UGF and Sec. II B for NUGF. In Sec. II A, we first describe the development of the AE model with UGF. We then perform stability analyses using

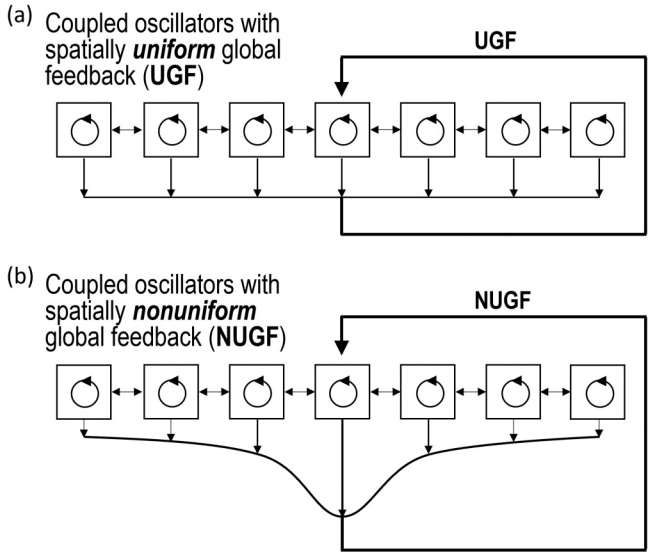


FIG. 3. Schematic diagrams of coupled oscillators with global feedback. (a) Spatially uniform global feedback (UGF). (b) Spatially nonuniform global feedback (NUGF). In the chemical reaction experiments [Figs. 1(a) and 1(b)], external global feedback loops were added in the setups, while in the cardiac myocytes [Fig. 1(c)], the transmembrane volage is uniform throughout the cell membrane and mediates a global feedback loop. There are no such direct global feedback loops in *E. coli* (Fig. 2). However, in chemical or biochemical reactions, reactants diffuse in space, and thus the feedback loops are not localized but spatially distributed. For faster diffusion, the feedback's influence is further away in space. At the limit of infinitely fast diffusion, the reactants affect other reactants equally in space, forming a UGF loop. Therefore, under a finite diffusion rate, the feedback loops can be considered as NUGF loops in which the feedback effects become weaker further away in space. In this study, we use a Gaussian distribution to represent the nonuniform feedback strength.

the AE model for stability of the uniform steady-state solutions and that for the front solutions in 1D media. For 2D media, we perform stability analyses for curved fronts. These stability analyses for 1D and 2D media reveal the roles of UGF and provide mechanistic insights into alternating pattern formation and selection in the media. In Sec. II B, we add a Gaussian-weighted feedback terms into the AE model to form an AE with NUGF. Similar to the UGF case, we perform stability analyses in both 1D and 2D media to reveal the roles of NUGF in alternating pattern formation and selection. Under both UGF and NUGF, we use more detailed reaction-diffusion models, including the periodically paced Fitzhugh-Nagumo (FHN) model, the BZ reaction model, and the carbon monoxide (CO) oxidation model (see the Appendix for details) to validate the theoretical predictions of the AE models.

II. RESULTS

A. Pattern stability and formation in media with spatially uniform global feedback

In this section, we perform both mathematical analysis and computer simulations to investigate the mechanisms of alternating pattern formation under UGF. We first use an AE

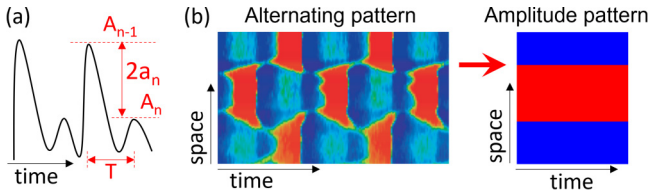


FIG. 4. Conversion of alternating stripes to stationary amplitude stripes. (a) Schematic plot for defining the amplitude of a period-2 state. A_n is the peak value of the nth cycle and a_n is defined as the amplitude of the period-2 state. T is the period. (b) Conversion of a continuous recording into an amplitude recording, transforming an alternating (period-2) cluster pattern into a stationary cluster pattern.

for theoretical analysis and computer simulations of the AE and other models to verify the theoretical predictions.

1. The amplitude equation with UGF

In previous studies [46,47], Echebarria and Karma developed an AE model to describe the dynamics of the action potential duration (APD) alternans in cardiac conduction, which was later modified or extended to describe intracellular calcium alternans as well as its coupling with APD alternans [43,48,49]. For the heart, in each heartbeat, cardiac myocytes are excited with an action potential, with APD being a quantity to describe their behaviors. Under normal conditions, APD remains roughly the same. Under disease conditions, a period-2 behavior, called alternans, is widely observed and linked to sudden cardiac death [19]. During alternans, APD exhibits a long-short-long-short periodic pattern. In the original study of Echebarria and Karma [46], they defined a new variable called alternans amplitude as $a_n = (-1)^n(\mathrm{APD}_n - \mathrm{APD}_{n-1})/2$ with $(-1)^n$ to ensure that a_n remains the same sign (either positive or negative) during alternating beats. They then derived an AE to allow analytical treatments to describe the alternans dynamics during conduction in a 1D cable, i.e., $\frac{\partial a}{\partial t} = \alpha a - \beta a^3 - \int_0^x \frac{dx'}{\Lambda} a(x') - w\frac{\partial a}{\partial x} + \xi^2 \frac{\partial^2 a}{\partial x^2}$. In this equation, α and β are two parameters derived from APD restitution properties. ξ^2 is the diffusion constant related to the electrical coupling strength of the myocytes. The third and fourth terms in the equation are related to action potential conduction. Note that a_n is a time-discretized variable, and they assumed $t = nT$ (T is the activation period) as a continuous variable to obtain the time-continuous partial differential equation. In a later study by Shiferaw and Karma [43], they phenomenologically extended this equation to describe the subcellular calcium alternans dynamics. The alternans amplitude was then defined as [Fig. 4(a)] $a_n = (-1)^n(A_n - A_{n-1})/2$, in which A_n is the peak of calcium concentration in the myocyte. Using this transformation, one transforms the alternating spatial pattern into a stationary spatial pattern [Fig. 4(b)]. Without wave conduction, the AE is then a standard bistable equation [50], i.e., $\frac{\partial a}{\partial t} = \alpha a - \beta a^3 + \nabla^2 a$, and we have used this equation to investigate alternans dynamics in the absence of conduction [48,49].

In this study, we extend this equation to describe the alternating (temporal period-2) pattern dynamics in periodically-paced excitable media or oscillatory media. Instead of deriving the AE based on the reaction-diffusion systems as did

by Echebaria and Karma for cardiac conduction, we simply take the bistable equation and add a feedback term into the equation. We define the amplitude of the period-2 state as $a_n = (-1)^n(A_n - A_{n-1})/2$ with A_n being the peak of a reactant in the reaction-diffusion system. For the model with UGF, the AE is as follows:

$$\frac{\partial a}{\partial t} = \alpha a - \beta a^3 + \nabla^2 a + \gamma(\bar{a} - a_{\text{ref}}), \tag{1}$$

where the last term is the UGF with $\bar{a}(t) = \frac{1}{L}\int_0^L a(x,t)dx$ for 1D media or $\bar{a}(t) = \frac{1}{L^2}\iint_0^L a(x,y,t)dxdy$ for 2D media. L is the length of the 1D media or the side length of the 2D media. a_{ref} is the reference state for the feedback, γ is the feedback strength, and the feedback is negative when $\gamma < 0$ and positive when $\gamma > 0$. We set $a_{\text{ref}} = 0$ based on the following observations: (i) $a = 0$ is a steady state of the standard bistable equation and remains a steady state of Eq. (1) since $a_{\text{ref}} = 0$; (ii) in a typical nonuniform alternating pattern, such as discordant subcellular calcium alternans [43], $\bar{a} = 0$ due to spatial symmetry of the pattern, and choosing $a_{\text{ref}} = 0$ does not change the nonuniform solution; and (iii) it is more convenient for analytical treatment as shown in the sections below. However, $a_{\text{ref}} \neq 0$ may also be justifiable and appropriate choices.

2. *Uniform solutions and their stabilities in 1D media*

The nonspatial system,

$$\frac{da}{dt} = \alpha a - \beta a^3, \tag{2}$$

has one steady-state solution $a_s = 0$ when $\alpha < 0$, and three steady-state solutions when $\alpha > 0$, i.e.,

$$a_s = \pm\sqrt{\alpha/\beta} \quad \text{and} \quad a_s = 0. \tag{3}$$

The stabilities of the three states are determined by their eigenvalues:

$$\lambda = \begin{cases} \alpha, & a_s = 0 \\ -2\alpha, & a_s = \pm\sqrt{\alpha/\beta} \end{cases} \tag{4}$$

Therefore, when $\alpha < 0$, there is a single steady-state solution ($a_s = 0$) which is stable since $\lambda = \alpha < 0$. When $\alpha > 0$, there are three steady-state solutions. Since $\lambda = \alpha > 0$, the zero steady-state solution ($a_s = 0$) becomes unstable, and the nonzero solutions ($a_s = \pm\sqrt{\alpha/\beta}$) are stable since $\lambda = -2\alpha < 0$. The nonspatial system with feedback is (since $a_{\text{ref}} = 0$)

$$\frac{da}{dt} = \alpha a - \beta a^3 + \gamma a \tag{5}$$

which has one steady-state solution $a_s = 0$ when $\alpha + \gamma < 0$, and three steady-state solutions when $\alpha + \gamma > 0$, i.e.,

$$a_s = \pm\sqrt{(\alpha+\gamma)/\beta} \quad \text{and} \quad a_s = 0. \tag{6}$$

The eigenvalues are

$$\lambda = \begin{cases} \alpha + \gamma, & a_s = 0 \\ -2(\alpha+\gamma), & a_s \neq 0 \end{cases} \tag{7}$$

This implies that with the presence of the feedback loop, the steady states and their stabilities are altered. The bifurcation from the monostable state to the bistable state occurs when $\alpha = -\gamma$, indicating that a negative feedback loop delays the bifurcation (occurring at $\alpha > 0$) but a positive feedback loop promotes the bifurcation (occurring at $\alpha < 0$).

The steady-state solutions of the nonspatial system [Eq. (6)] are also the homogeneous steady-state solutions of the spatial system Eq. (1). Using linear stability analysis, i.e., inserting $a(x,t) = a_s + \eta e^{\lambda t + ikx}$ into Eq. (1), one obtains the following equation for λ:

$$\lambda e^{ikx} = \left(\alpha - 3\beta a_s^2 - k^2\right)e^{ikx} + \frac{\gamma}{L}\int_0^L e^{ikx}dx. \tag{8}$$

When $k = 0$, Eq. (8) becomes $\lambda = \alpha - 3\beta a_s^2 + \gamma$. When $k > 0$, it becomes $\lambda = \alpha - 3\beta a_s^2 - k^2$ since the integral term is zero under the periodic boundary condition. Therefore, one obtains the eigenvalues for $a_s = 0$ as

$$\lambda_k = \begin{cases} \alpha + \gamma, & k = 0 \\ \alpha - k^2, & k > 0 \end{cases} \tag{9}$$

and for $a_s = \pm\sqrt{(\alpha+\gamma)/\beta}$ as

$$\lambda_k = \begin{cases} -2(\alpha+\gamma),\ w & k = 0 \\ -2\alpha - 3\gamma - k^2, & k > 0 \end{cases} \tag{10}$$

According to Eq. (9), for the uniform solution $a_s = 0$, the zero-mode ($k = 0$) is unstable when $\gamma > -\alpha$ (or $\alpha > -\gamma$). However, for the nonzero Fourier modes ($k > 0$), it becomes unstable when $\alpha > k^2$, which implies that when $\alpha > 0$, there are always unstable modes. Therefore, for $\gamma < 0$, the uniform solution ($a_s = 0$) is stable when $\alpha < 0$. This is because when $\alpha > 0$, there are always nonzero Fourier modes that are unstable. For $\gamma > 0$, the uniform solution ($a_s = 0$) is stable when $\alpha < -\gamma$. This is because when $\alpha > -\gamma$, the zero mode loses stability. Therefore, the stable region for $a_s = 0$ is the olive region in Fig. 5(a). For a given α, the minimum length is $L_c = \frac{2\pi}{\sqrt{\alpha}}$ for periodic boundary conditions based on $\alpha - k^2 = 0$ (for a periodic boundary, $k = \frac{2\pi n}{L}$, with n being an integer).

According to Eq. (10), for the uniform solution $a_s = \pm\sqrt{(\alpha+\gamma)/\beta}$, the zero-mode is unstable when $\gamma < -\alpha$ (or $\alpha < -\gamma$). For the nonzero modes, they are unstable when $-2\alpha - 3\gamma > k^2$, implying that when $\alpha < -1.5\gamma$, there are always unstable modes. Following the same reasoning as for the solution $a_s = 0$, the solutions $a_s = \pm\sqrt{(\alpha+\gamma)/\beta}$ are stable when $\alpha > -1.5\gamma$ for $\gamma < 0$ [gray region in Fig. 5(a)] and when $\alpha > -\gamma$ for $\gamma > 0$ [cyan region in Fig. 5(a)].

3. *Front solutions and stability in 1D media*

Without the feedback term ($\gamma = 0$), Eq. (1) is the standard form of a bistable equation [50], and in an infinitely long 1D medium or cable, it has the following front solution:

$$a(x,t) = \sqrt{\frac{\alpha}{\beta}}\tanh\left(\sqrt{\frac{\alpha}{2}}x\right) \tag{11}$$

which exists when $\alpha > 0$ and $\beta > 0$. Due to the symmetry of the standard form of the bistable equation, the front velocity is zero and its stability is neutral. When $\gamma \neq 0$, Eq. (11) is still a solution of Eq. (1) [the solid curve in Fig. 5(b)] since $\bar{a} = 0$ and $a_{\text{ref}} = 0$. However, the front solution can be stable or unstable depending on the sign of γ. Assuming that there is

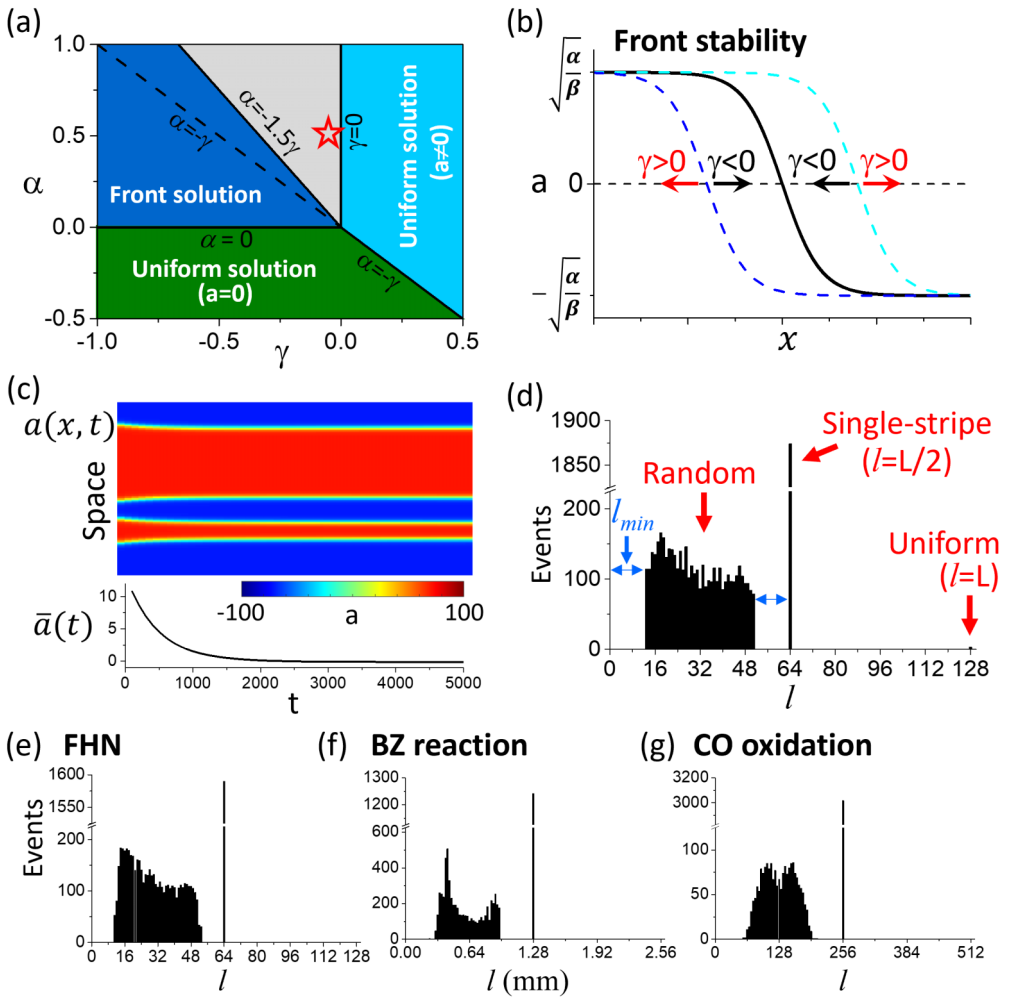


FIG. 5. Front dynamics in a 1D medium with UGF. (a) Phase diagram in α-γ space from the stability analyses of the bistable equation with UGF [Eq. (1)]. The $\alpha = -\gamma$ line is the stability boundary of the zero mode of $a_s = 0$, and the $\alpha = 0$ line is the stability boundary of the nonzero mode of $a_s = 0$. The $\alpha = -1.5\gamma$ line is the stability boundary of the nonzero mode of $a_s = \pm\sqrt{(\alpha+\gamma)/\beta}$. The $\gamma = 0$ line is the stability boundary of the front solution. The olive region exhibits stable zero uniform solutions (no alternating patterns). The blue region exhibits stable front solutions (corresponding to spatiotemporally alternating patterns). The cyan region exhibits stable nonzero uniform solutions (corresponding to spatially uniform alternating patterns). The gray region exhibits both stable front solutions and nonzero uniform solutions. (b) Schematic plot of the effects of UGF on the front stability. Arrows indicate the moving directions of the front when it is away from the steady-state front solution. (c) A time-space plot of a (see color bar) and the corresponding $\bar{a}$ vs t for a random initial condition. (d) Domain size distribution from 2000 simulations with random initial conditions in a 1D medium. Domain sizes are calculated at $t = 50\,000$. Double arrows mark minimum cluster size $l_{\min}$ and open arrow highlights the nonzero event number at $l = L$. Simulations in (c) and (d) are done using Eq. (1) with $\alpha = 0.5$, $\beta = 0.0001$, $\gamma = -0.012$ [star in (a)], and $L = 128$. (e)–(g) Domain size distributions of the FHN model ($L = 128$), the BZ reaction model ($L = 2.56$ mm), and the CO oxidation model ($L = 512$).

a small shift of the front solution [dashed curves in Fig. 5(b)], then $\gamma\bar{a} = \xi \neq 0$. We assume that ξ is a constant, and we rewrite Eq. (1) as

$$\frac{\partial a}{\partial t} = \alpha a - \beta a^3 + \nabla^2 a + \xi \tag{12}$$

which can be rewritten as

$$\frac{\partial a}{\partial t} = -\beta(a-a_0)(a-a_1)(a-a_2) + \nabla^2 a \tag{13}$$

with the following front solution [50]:

$$a(x,t) = \frac{a_0+a_2}{2} + \frac{a_2-a_0}{2}\tanh\left[\sqrt{\frac{\beta}{2}}\frac{a_2-a_0}{2}(x-ct)\right] \tag{14}$$

and the front velocity c:

$$c = \sqrt{\frac{\beta}{2}}(a_0 - 2a_1 + a_2). \tag{15}$$

Although one can obtain a_0, a_1, and a_2 by analytically solving the cubic equation $\alpha a - \beta a^3 + \xi = 0$, the solutions are too complex to be useful. Assuming that ξ is a small constant, then one obtains approximately $a_0 \approx -\sqrt{\frac{\alpha}{\beta}} + \frac{\xi}{2\alpha}$, $a_1 \approx -\frac{\xi}{\alpha}$, and $a_2 \approx \sqrt{\frac{\alpha}{\beta}} + \frac{\xi}{2\alpha}$. Using these approximated solutions, one obtains the front velocity from Eq. (15) as

$$c \approx \sqrt{\frac{\beta}{2}}\frac{3\xi}{\alpha} = \sqrt{\frac{\beta}{2}}\frac{3\gamma\bar{a}}{\alpha}. \tag{16}$$

With Eq. (16), one can now evaluate the stability of the steady-state front solution. For the front to be a steady state (not moving), $c = 0$ is required. This requires $\bar{a} = 0$. As illustrated in Fig. 5(b), when $\gamma < 0$ (negative feedback, black arrows), if a front is on the left side (dashed blue line) of the steady-state front solution, then $\bar{a} < 0$, which gives rise to $\gamma\bar{a} > 0$ and thus $c > 0$. This indicates that the front moves rightward. When a front is on the right side (dashed cyan line) of the steady-state front solution, then $c < 0$, and it moves leftward. In other words, when the initial front position is on either side of the steady-state front solution, it will move toward the steady state, and therefore the steady-state front solution is stable. When $\gamma > 0$ [red arrows in Fig. 5(b)], the feedback is positive, and following the same argument, the steady-state front solution is unstable.

Although the solution Eqs. (11) or (14) is accurate only for an infinitely long cable, the same stability argument can be extended to a finite cable with multiple fronts as long as the front velocity follows the same rule as in Eq. (16). Therefore, we can generalize the conclusion as that stable front solutions exist when $\gamma < 0$ and $\alpha > 0$. Note that we call the pattern in Fig. 4(b) a single-stripe pattern and the one in Fig. 5(c) is a multistripe pattern. In a single-stripe pattern, there are two opposite fronts.

4. Pattern selection in 1D media

Based on the spatial mode stability and the front stability analyses above, we obtain a complete phase diagram of the bistable equation with UGF for a 1D medium [Fig. 5(a)]: the olive region exhibits only the stable zero uniform solution, the cyan region exhibits only the stable nonzero uniform solutions, the blue region exhibits only the stable front solutions only, and the gray region includes both stable front solutions and nonzero uniform solutions. Therefore, when $\gamma < 0$ and $\alpha > 0$, spatial pattern formation occurs, and the specific pattern depends on initial conditions. Figure 5(c) shows an evolution of an example pattern starting from a random initial condition, which stabilizes with $\bar{a}$ approaching zero. The pattern includes four spatial domains (not five because of the periodic boundary condition) of different sizes. To show possible patterns in the cable, Fig. 5(d) shows a histogram of domain size from many simulations of the same cable with random initial conditions, showing that the domain sizes (l) can be $l_{\min} < l < \frac{L}{2} - l_{\min}$, $l = L/2$, and $l = L$. The 1D pattern is a combination of the allowed domain sizes, which is selected by satisfying $\sum_{k=1}^{K} l_k = L$ and $\bar{a} = 0$, where K is the total number of domains. We carry out simulations of 1D medium for the three reaction-diffusion models—the FHN model [Fig. 5(e)], the BZ reaction model [Fig. 5(f)], and the CO oxidation model [Fig. 5(g)]—and the domain size histograms are similar to that of the AE model. Note that it is unclear what determines the minimum domain size. In general, for a reaction-diffusion system, the source-sink relationship requires a domain to be sufficiently large to overcome the sink effect of its neighbors.

5. Curved front stability in 2D media

The 1D cable results can extend to a 2D medium into straight stripes with different stripe widths. However, other patterns may exist, i.e., patterns with curved fronts. To understand the curvature effect on the stability of patterns, we consider a single circular pattern in the medium and rewrite Eq. (1) using polar coordinates, i.e.,

$$\frac{\partial a}{\partial t} = \alpha a - \beta a^3 + \frac{1}{r}\frac{\partial a}{\partial r} + \frac{\partial^2 a}{\partial r^2} + \gamma(\bar{a} - a_{\text{ref}}). \tag{17}$$

The center of the circle is the origin of the coordinate system. As shown previously [48], the eikonal relationship can be used for the front velocity, i.e., $c = c_0 - \kappa$, where c_0 is the velocity of the planar front determined by Eq. (15) and $\kappa = \frac{1}{r}$ is the curvature. Then one has the velocity for the circular front as

$$c \approx \sqrt{\frac{\beta}{2}}\frac{3\gamma\bar{a}}{\alpha} - \frac{1}{r}. \tag{18}$$

The average amplitude $\bar{a}$ in the 2D medium is calculated as $\bar{a} \approx \sqrt{\frac{\alpha}{\beta}}(L^2 - 2\pi r^2)/L^2$ in which L is the side length and r is the radius of the circular front. The velocity of the circular front is $c \approx 3\gamma\sqrt{\frac{1}{2\alpha}}(1-2\pi r^2/L^2) - \frac{1}{r}$. When $c = 0$, the circular front is in an equilibrium state with the equilibrium radius R being solved from a cubic equation of the form $r^3 + pr + q = 0$. The properties of the solutions are determined by the sign of $\Delta = (\frac{q}{2})^2 + (\frac{p}{3})^3$, which is

$$\Delta = \left(\frac{L^2\sqrt{2\alpha}}{12\pi\gamma}\right)^2 - \left(\frac{L^2}{6\pi}\right)^3. \tag{19}$$

When $\Delta > 0$, there exists only one real solution [R_1 in Fig. 6(b)]. When $\Delta < 0$, there are three real solutions [labeled as R_1, R_2, and R_3 in Figs. 6(a) and 6(b)]: one solution is stable (solid) and the other two are unstable (dashed). When the initial radius r is smaller than R_3, the front shrinks and disappears. When $r > R_1$, the circular front expands and disappears. When $R_1 < r < R_3$, the front will approach the stable one (R_2). The critical medium size for the existence of a stable circular front is obtained by setting $\Delta = 0$ in Eq. (19), which gives rise to

$$L_c = -\frac{\sqrt{3\pi\alpha}}{\gamma} \tag{20}$$

and the critical radius of the front solution is

$$R_c = \sqrt[3]{-\frac{q}{2}} = \sqrt[3]{-\frac{L_c^2\sqrt{2\alpha}}{12\pi\gamma}} = \sqrt[3]{-\frac{\alpha\sqrt{2\alpha}}{4\gamma^3}}. \tag{21}$$

Note that for L_c and R_c to be positive, $\gamma < 0$ is required. In other words, the circular fronts are stable only when the feedback is negative, otherwise, they will diminish from the medium. Furthermore, a weaker feedback strength requires a larger tissue size to support the circular front.

To verify this simple theoretical prediction, we carry out simulations of Eq. (1) to determine the stability of a circular front in a 2D medium. An initial circular front is placed in the center of the medium and we change the radius r of the circular front to test its stability. The simulation results are shown in Fig. 6(b) with $\alpha = 0.5$ and $\gamma = -0.012$. When the medium size is smaller than the critical size L_c ($L_c \approx 182$ and $R_c \approx 42$), no circular fronts can exist in the medium. The L_c (and R_c) determined from the numerical simulation agrees

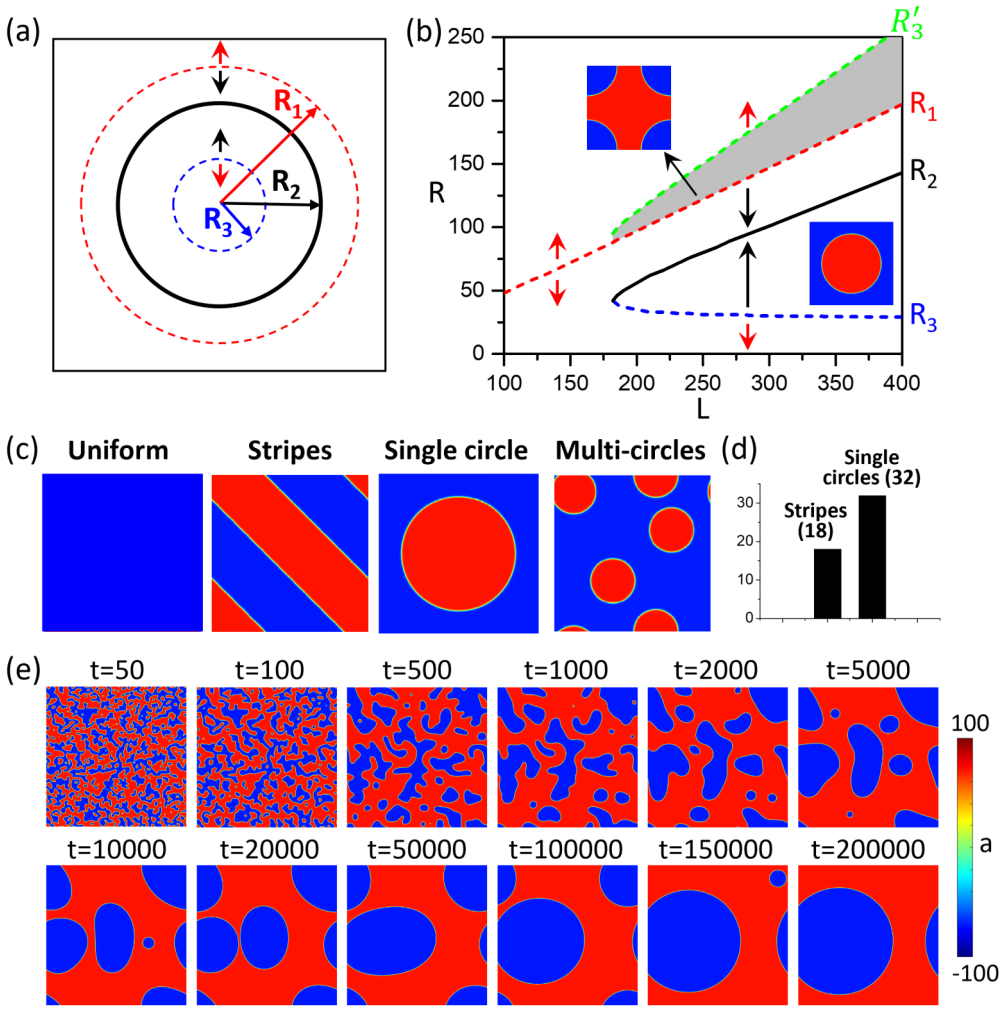


FIG. 6. Pattern selection and dynamics in 2D media of the AE model with UGF. (a) Schematic diagram showing stable (solid) and unstable (dashed) ring solutions. (b) Stable and unstable radii determined from numerical simulation of Eq. (1) using circular initial conditions. (c) Snapshots of different patterns from given initial conditions. (d) Bar graph showing selected patterns from simulations of Eq. (1) with random initial conditions from a total of 50 trials. Although all four patterns are solutions, we only observed two patterns for the 50 trials. (e) Consecutive snapshots taken between $t = 50$ (first panel) and $t = 2 \times 10^5$ (last panel) showing evolution of a random initial pattern into a stable single-circle pattern. Simulations of Eq. (1) were done in $L \times L$ 2D media. $L = 400$ for (c) and (d), and $L = 1000$ for (e).

well with the predicted values of Eqs. (20) and (21), which give rise to $L_c \approx 180.9$ and $R_c \approx 41.7$. When the medium size is greater than L_c, if the initial radius of the circular front is greater than R_3 and smaller than R_1, the front will always approach the stable circular front solution R_2. When $r < R_3$, the front will disappear from the medium, leading to a uniform pattern. However, when $R_1 < r < R_3^{'}$, we observe a new pattern, which is just a mirror image of the circular center because we use periodic boundary conditions. $R_3^{'}$ is simply a mirror of R_3.

A 2D medium can also have multiple circular fronts. In this case, the average amplitude $\bar{a}$ is calculated as $\bar{a} \approx \sqrt{\frac{\alpha}{\beta}}(L^2 - N2\pi r^2)/L^2$, where N is the number of circular fronts. Following the same argument, the critical medium size for N circular fronts in the same medium is determined by $\Delta = (\frac{L^2\sqrt{2\alpha}}{12\pi N\gamma})^2 - (\frac{L^2}{6\pi N})^3 = 0$, leading to $L_c = -\frac{\sqrt{3\pi N\alpha}}{\gamma}$. Based on Eq. (21), $R_c = \sqrt[3]{-\frac{L_c^2\sqrt{2\alpha}}{12\pi N\gamma}} = \sqrt[3]{-\frac{\alpha\sqrt{2\alpha}}{4\gamma^3}}$, which is the same as that for the single-circle pattern. In other words, for a 2D medium to fit in N circular fronts, its minimum area is N times the area of the single circular front, which is not surprising.

For a multiple-circle pattern, the positions of the circles do not need to be spatially periodic, but all the circles must be the same size for a stable pattern. This is because when the front is stable, the conduction velocity must be zero, and based on Eq. (18), only a single r value can satisfy this requirement. In other words, if the radii of the circles are different, they cannot simultaneously satisfy $\sqrt{\frac{\beta}{2}}\frac{3\gamma\bar{a}}{\alpha} - \frac{1}{r} = 0$ unless all the circles have the same radius r. One can extend the same reasoning to conclude that stable nonuniform curved front solutions cannot exist because the curvature (κ) has to be uniform to satisfy $\sqrt{\frac{\beta}{2}}\frac{3\gamma\bar{a}}{\alpha} - \kappa = 0$ everywhere in the curved front. This requirement can only be satisfied when the front is a straight line ($\kappa = 0$) or a circle whose κ is the same everywhere.

Therefore, besides the homogeneous pattern, a 2D homogeneous medium can support stable straight fronts (stripes)

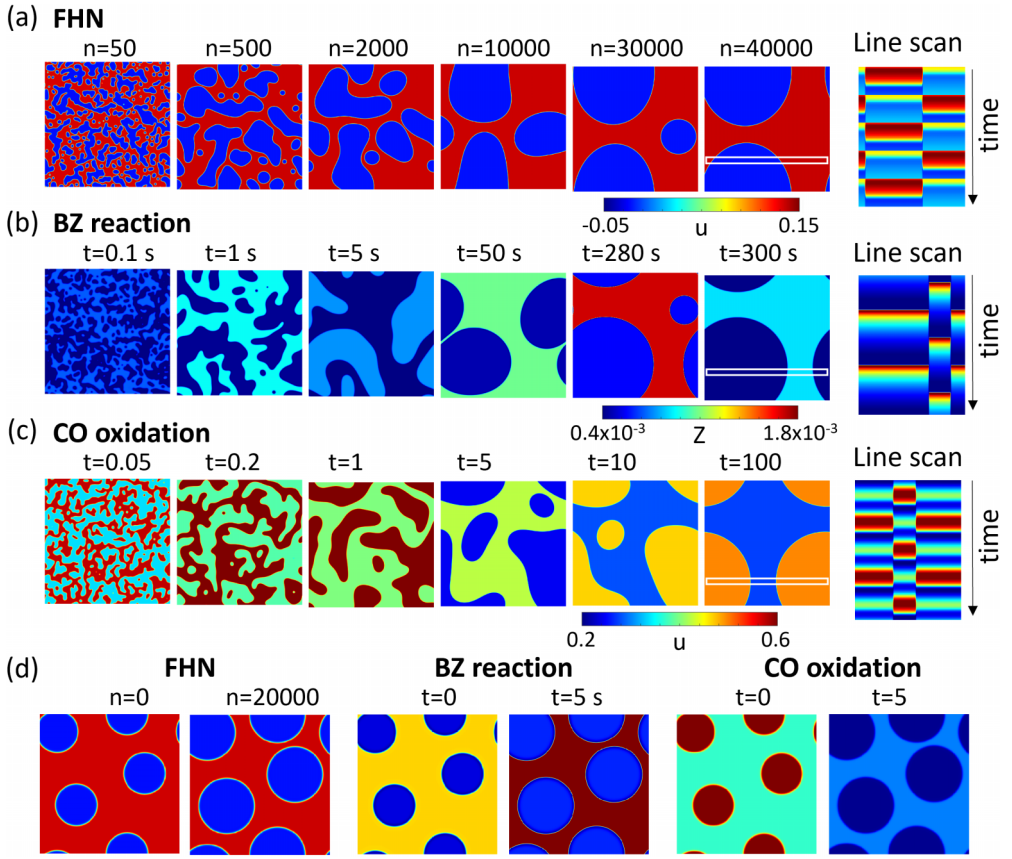


FIG. 7. Pattern selection in 2D media with UGF. (a) The periodically paced FHN model with a delayed UGF ($L = 1000$). First 6 panels: Snapshots in a 2D medium showing evolution of a random initial pattern into a stable single-circle alternating pattern. n is the cycle number, corresponding to $t = nT$. Last panel: Line scan taken from the white line as marked on the last snapshot showing the alternating patterns. (b) Same as (a) but for the BZ reaction model with UGF ($L = 20$ mm). (c) Same as (a) but for the CO oxidation model with a delayed UGF ($L = 4000$). (d) Initially given (left) and final stable (right) 4-circle alternating patterns in 2D media of the three models as marked. Note that in (a)–(c), the final state (the last snapshot) of each model looks like a complex pattern but is in fact a single-circle pattern because of the periodic boundary condition. See color bars for the variable plotted and color scales.

and single or multiple circular fronts. The stripes can be with different stripe widths, a direct extension of the 1D cable patterns. The circular fronts must have the same radius to satisfy the front stability requirement. Note that for stripe patterns, $\bar{a} = 0$ is required, but for circular cluster patterns, since $\sqrt{\frac{\beta}{2}\frac{3\gamma\bar{a}}{\alpha}} - \kappa = 0$ is required, therefore, for a steady-state circular pattern, $\bar{a} \neq 0$.

6. Pattern selection and stability in 2D media

Based on the theoretical arguments above, in a 2D medium, it can exhibit uniform solutions, straight stripes with different stripe widths (direct extension of the 1D cable patterns), single-circle patterns, and multicircle patterns with the same size circles. The selection of the patterns depends on the choice of parameters, medium sizes, and initial conditions. For example, when $\alpha = 0.5$ and $\gamma = -0.012$ [star in Fig. 5(a)] are used, the medium can exhibit all four patterns when $L > L_c$ [Fig. 6(c)]. However, if we use random initial conditions, the probability of selecting the uniform solution or multicircle patterns is extremely low. For example, in a total of 50 trials, we obtained 18 stripe patterns and 32 single-circle patterns for a medium size $L = 400$ [Fig. 6(d)], and no uniform or multicircle patterns were observed. Figure 6(e) shows an example in a larger medium ($L = 1000$) in which the initial random initial pattern evolves into a single-circle pattern albeit very slowly. In the evolution process, the smallest circle in the medium disappears first, and this process repeats, leaving only one circle to survive to the very end and stabilized.

To verify the theoretical predictions of the AE model, we carry out simulations using three different models (see the Appendix): (i) Periodically paced FHN model with a delayed UGF; (ii) the BZ reaction with an instantaneous UGF; and (iii) the CO oxidation model with a delayed UGF. Figures 7(a)–7(c) show snapshots (left panels) and line scans (rightmost panel) from 2D media starting from random initial conditions. The final stable patterns are single-circle patterns for all three models. Indeed, if we preset the initial condition to a multicircle pattern with the same radius, all three models can support stable multicircle patterns [Fig. 7(d)].

B. Pattern formation and stability in media with spatially nonuniform global feedback

As shown in our previous study [45], when the global feedback is spatially nonuniform, a transition from alternating stripes to alternating labyrinths occurs. In this section, we

extend our previous work to perform a more detailed stability analysis and carry out simulations using different models to validate the theoretical predictions.

1. The amplitude equation with NUGF

In addition to the UGF, here we add a spatially Gaussian-weighted global feedback loop to investigate the pattern dynamics. After adding a spatially Gaussian-weighted global feedback term to Eq. (1), the differential equation becomes

$$\frac{\partial a}{\partial t} = \alpha a - \beta a^3 + \nabla^2 a + \gamma(\bar{a} - a_{\text{ref}}) + \varepsilon(\bar{a}_g - a_{\text{ref}}), \quad (22)$$

where $\bar{a}_g$ is the Gaussian-weighted spatial average of a, defined for 1D media as

$$\bar{a}_g(x,t) = \frac{1}{N\sqrt{2\pi}\sigma} \int_{-\frac{L}{2}-x}^{\frac{L}{2}-x} a(x',t) e^{-(x'-x)^2/2\sigma^2} dx' \quad (23)$$

and for 2D media as

$$\bar{a}_g(x,y,t) = \frac{1}{N2\pi\sigma^2} \iint_{-\frac{L}{2}-x,\ -\frac{L}{2}-y}^{\frac{L}{2}-x,\ \frac{L}{2}-y} a(x',y',t) \times e^{-[(x'-x)^2+(y'-y)^2]/2\sigma^2} dx'dy'. \quad (24)$$

N in Eqs. (23) and (24) is the normalization constant satisfying $\frac{1}{N\sqrt{2\pi}\sigma}\int_0^L e^{-x^2/2\sigma^2}dx = 1$ for 1D media and $\frac{1}{N2\pi\sigma^2}\iint_0^L e^{-[x^2+y^2]/2\sigma^2}dxdy = 1$ for 2D media. When $L \gg \sigma$, $N \to 1$. For simplicity, we set $a_{\text{ref}} = 0$ as in the UGF case.

2. Stability of the uniform steady states in 1D media

Similar to the UGF case, we first invesitgate the stability of the uniform steady states. Inserting $a(x,t) = a_s + \eta e^{\lambda t + ikx}$ into Eq. (22), then the Gaussian term becomes

$$\bar{a}_g(x,t) = \frac{1}{N\sqrt{2\pi}\sigma} \int_{-\frac{L}{2}-x}^{\frac{L}{2}-x} (a_s + \eta e^{\lambda t + ikx'}) e^{-(x'-x)^2/2\sigma^2} dx'. \quad (25)$$

For an arbitrary size L, Eq. (25) cannot be explicitly integrated. When the 1D medium is infinitely large, i.e., $L \to \infty$ (or practically $L \gg \sigma$), Eq. (25) can be integrated, resulting in $\bar{a}_g(x,t) = a_s + \eta e^{\lambda t + ikx}$. Then the eigenvalue λ for the zero uniform steady state ($a_s = 0$) as a function of the wave number k is

$$\lambda_k = \begin{cases} \alpha + \gamma + \varepsilon, & k = 0 \\ \alpha - k^2 + \varepsilon e^{-\frac{\sigma^2 k^2}{2}}, & k > 0 \end{cases} \quad (26)$$

When $\varepsilon = 0$, Eq. (26) is simply Eq. (9). When $\varepsilon > 0$, λ_k decreases with k monotonically with the most unstable mode to be $k = 0$. The $k = 0$ mode is unstable when $\alpha + \varepsilon > 0$ or $\alpha + \gamma + \varepsilon > 0$. When $\varepsilon < 0$, however, λ_k can become a nonmonotonic function of k [Fig. 8(a)]. From Eq. (26), one obtains the k value at the local maximum of λ_k, i.e., $k_{\max} = \sqrt{\frac{-2}{\sigma^2}\ln\frac{-2}{\varepsilon\sigma^2}}$ (and $\varepsilon\sigma^2 < -2$ is required for the value of $k_{\max}$ to be a real number). Inserting $k = k_{\max}$ into Eq. (26) and setting $\lambda_k = 0$, one obtains the stability boundary as

$$\alpha = \frac{2}{\sigma^2}\left(1 - \ln\frac{-2}{\varepsilon\sigma^2}\right). \quad (27)$$

Equation (27) can also be rewritten as $\varepsilon = \frac{-2}{\sigma^2}e^{(\frac{\alpha\sigma^2}{2}-1)}$. When $\sigma \to \infty$, the right side of Eq. (27) approaches zero and thus the stability boundary becomes $\alpha = 0$, which is the same as in the UGF case. For a finite σ, the stability boundary is $\alpha > 0$, indicating that the Gaussian-weighted feedback term stabilizes the uniform steady state.

We plot Eq. (27) in the parameter plane of σ and ε for $\alpha = 0.5$ in Fig. 8(b) (the green curve). The zero steady-state solution ($a_s = 0$) is unstable above this boundary. Once this steady state is unstable, nonuniform solutions emerge in the system [48,49]. In other words, nonuniform solutions exist above the green curve. Note that in this symmetric bistable system, a nonuniform solution is just a front solution with zero front speed.

For the nonzero uniform steady state, the solutions become $a_s = \pm\sqrt{(\alpha + \gamma + \varepsilon)/\beta}$, and the eigenvalues are

$$\lambda_k = \begin{cases} -2(\alpha + \gamma + \varepsilon), & k = 0 \\ -2\alpha - 3\gamma - 3\varepsilon - k^2 + \varepsilon e^{-\frac{\sigma^2 k^2}{2}}, & k > 0 \end{cases} \quad (28)$$

Similar to the case of $a_s = 0$, by inserting $k = k_{\max} = \sqrt{\frac{-2}{\sigma^2}\ln\frac{-2}{\varepsilon\sigma^2}}$ into Eq. (28) and setting $\lambda_k = 0$, one obtains the stability boundary in the parameter space as

$$\alpha = -\frac{3}{2}(\gamma + \varepsilon) - \frac{1}{\sigma^2}\left(1 - \ln\frac{-2}{\varepsilon\sigma^2}\right). \quad (29)$$

When $\sigma \to \infty$, Eq. (29) becomes $\alpha = -\frac{3}{2}(\gamma + \varepsilon)$, which, when $\varepsilon = 0$, becomes the same stability boundary condition as in the UGF case [Eq. (28) is the same as Eq. (10) when $\varepsilon = 0$]. We plot this boundary for $\alpha = 0.5$ in Fig. 8(b) (the red curve). The nonzero uniform steady-state solutions are unstable below this boundary.

Note that the eigenvalues in Eqs. (26) and (28) were obtained under the condition of $L \gg \sigma$ (or $L \to \infty$). When $\sigma \gg L$ (or $\sigma \to \infty$), for which the feedback can be treated as UGF, the stability conditions of the uniform steady states can be obtained by replacing γ with $\gamma + \varepsilon$ in Eqs. (9) and (10) or setting $\sigma \to \infty$ in Eqs. (26) and (28).

3. Stability of front solutions in 1D media

With the presence of the Gaussian-weighted feedback term, we are not able to obtain the front solution and analyze its stability as in the UGF case. Nonetheless, we obtain $a_s(x)$ numerically using the 1D medium for a given σ. Without the feedback term in Eqs. (1) or (22), the stability of the front solutions is neutral. As shown in our previous studies [44,49], a negative global feedback loop stabilizes the front solutions under UGF.

Differing from the UGF case, with a negative NUGF, the front solutions can become unstable, however stability analysis is nontrivial. Here we only determine the stability of single-stripe solutions using numerical simulations of the 1D AE model, i.e., we use a single-stripe initial condition to examine if the system stays at a single-stripe solution or not. If the system decays into a multistripe solution, we call the single-stripe solution unstable. The blue line in Fig. 8(b) is the stability boundary determined using this method. Above this line the single-front solution is stable, but below this line the single-front solution is unstable. Figures 8(c) and 8(d) show

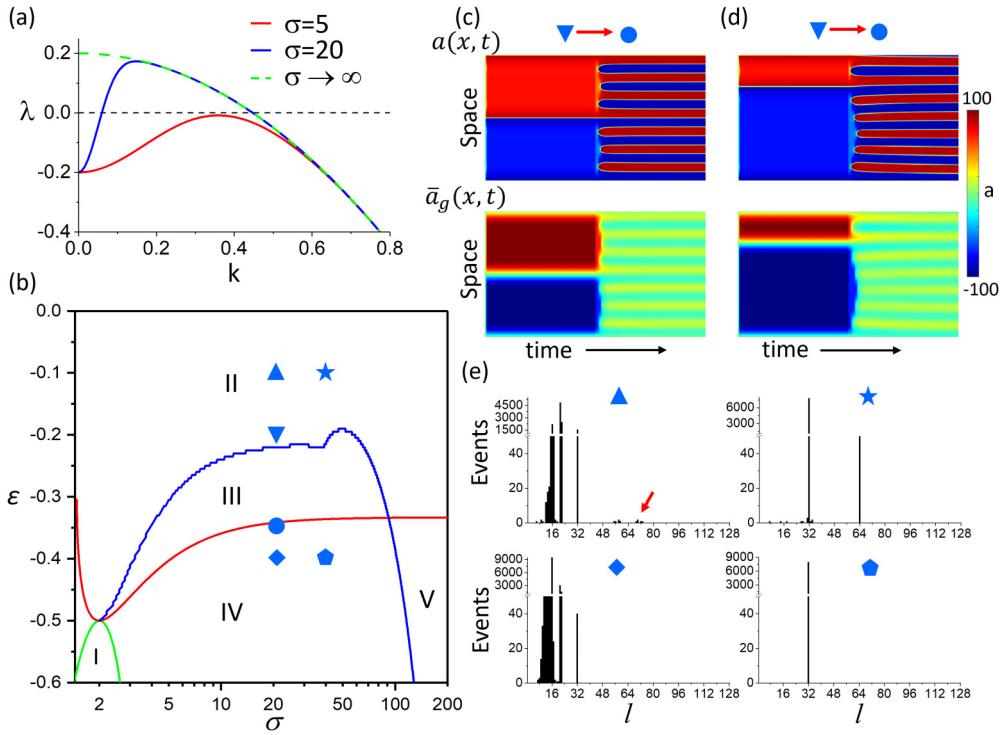


FIG. 8. Stability of uniform steady states and front solutions in 1D media of the AE model with NUGF. (a) The eigenvalue λ vs the wave number k for the zero steady-state solution [Eq. (26)] for different σ as marked. $\alpha = 0.2$, $\gamma = 0$, and $\varepsilon = -0.4$. (b) Stability boundaries on the σ-ε plane for the zero steady-state solution (green), nonzero uniform steady-state solution (red) and single-stripe front solution (blue) obtain with $L = 400$. The stability boundaries divide the plane into five regions with distinct patterning dynamics as described in detail in the main text. (c) Time-space plots for an example showing a stable single-stripe front solution ($\varepsilon = -0.2$ and $\sigma = 20$, downward triangle) transition to a multistripe solution ($\varepsilon = -0.35$ and $\sigma = 20$, circle). $L = 400$. Upper: Time-space plot of a; lower: time-space plot of $\bar{a}_g$. (d) Same as (c) but from a different initial condition. (e) Histograms of domain size of steady-state patterns for 2000 random initial conditions. $L = 128$. The parameters are taken from the locations marked by the corresponding symbols in (b). The four parameter sets (σ, ε) are (20, –0.1), (40, –0.1), (20, –0.4), and (40, –0.4).

examples in which ε is switched from -0.2 (above the boundary, down triangle) to -0.35 (below the stability boundary, circle) at $t = 1000$; the single-front solutions remain stable before the switch but decay into multistripe patterns after the switch. Note that under UGF, single-stripe patterns with $l > L/2$ cannot exist; however, this is no longer the case under NUGF [$l > L/2$ (blue region) exists in Fig. 8(d)].

4. Pattern selection in 1D media

Similar to the UGF case, one can predict pattern behaviors under NUGF based on stability boundaries as shown in Fig. 8(b). In region I (under green curve), the system always stays at the zero uniform steady state ($a_s = 0$), and thus there is no pattern. In region II, the nonzero uniform state is stable, and the single-stripe solution and multistripe solutions are all stable. In region III, the nonzero uniform steady state is stable but the single-stripe solution is unstable (unless the medium is sufficiently small). In region IV, both the nonzero uniform steady-state solutions and the single-stripe solution are unstable. In region V, the nonzero uniform steady state is unstable but the single-stripe pattern is stable. The pattern dynamics exhibit some difference from the UGF case, which are as follows:

(i) Under UGF, at steady state, $\bar{a} = 0$ is required. This requirement blocks the selection of the domain size $\frac{L}{2} < l < L$. However, under NUGF, $\bar{a}_g$ is a function of space [Figs. 8(c) and 8(d)], and thus $\bar{a}_g = 0$ is no longer applicable. The domain size $\frac{L}{2} < l < L$ becomes possible. For example, in Fig. 8(d) before the parameter switch, the domain sizes are $l \approx L/4$ and $l \approx 3L/4$. In the first panel of Fig. 8(e), there are domain sizes $l > L/2$.

(ii) Under UGF, a single-stripe pattern ($l = L/2$) is always stable, but it is no longer true under NUGF. With a sufficiently strong feedback strength ε and proper width σ of the Gaussian function [below the blue curve in Fig. 8(b)], the single-stripe pattern is unstable when the medium size is larger than the critical value. In Fig. 8(e), the domain sizes in the two panels with $\varepsilon = -0.4$ are much smaller than $L/2$.

(iii) Under UGF, the domain size is random as long as $\bar{a} = 0$ is satisfied (see the histograms in Fig. 5). Under NUGF, as the feedback strength increases, the pattern becomes less and less random. At large feedback strength, only periodic patterns exist. For example, in Fig. 8(e), all patterns resulting from the 2000 random initial conditions are the same periodic pattern with a domain size $l = L/4$. Note that even under strong feedback, if σ is also large, then the NUGF is close to UGF, and the domain sizes become more random.

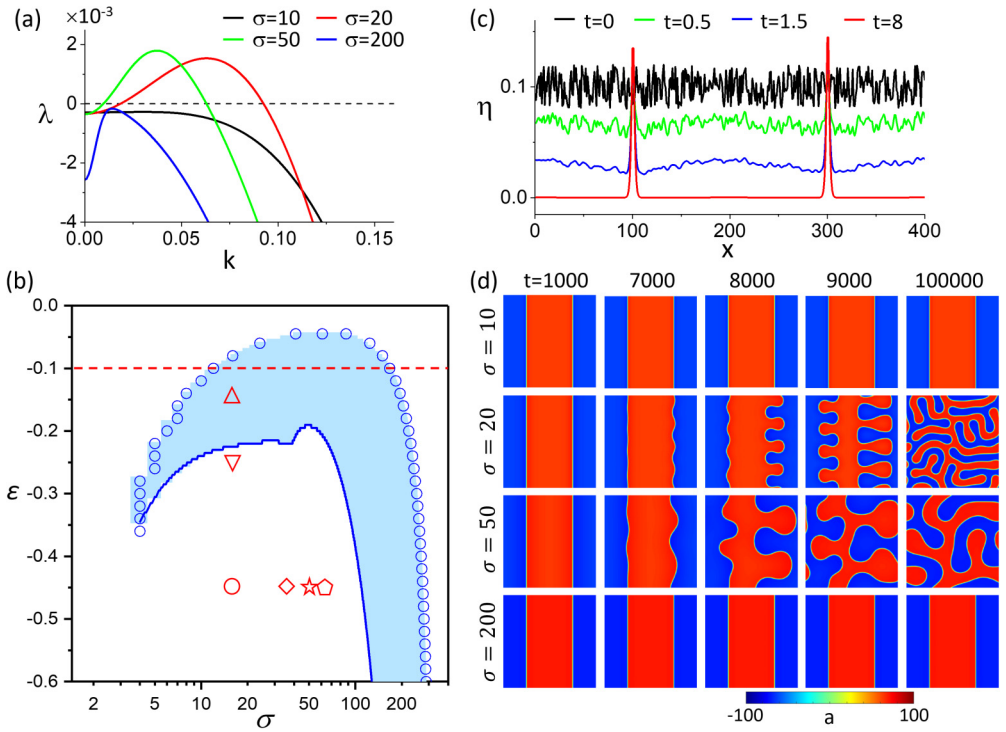


FIG. 9. Front instability in 2D media of the AE model with NUGF. (a) Lyapunov exponent λ vs wave number k calculated using Eqs. (31) and (32) for the single-stripe front solution for different σ values. (b) Stability boundaries in the σ-ε plane. The cyan region is where the single-stripe front solutions are transversely unstable. The upper boundary was determined by calculating the Lyapunov exponent using Eqs. (31) and (32). Blue circles on the upper boundary mark the boundary determined from direct 2D simulations [examples shown in (d)]. The blue line is a replot of the blue line in Fig. 8(b). (c) $\eta(x,t)$ at different time points for the case of $\sigma = 50$. (d) Snapshots of a in a 400×400 medium at different time points and σ values as marked. The initial condition ($t = 0$) is a single-stripe front solution (pattern in the first column). A small random perturbation is given at $t = 1000$.

5. *Front instability and pattern dynamics in 2D media*

For the stability of the uniform steady-state solutions in a 2D medium, one simply replaces k^2 by $k_x^2 + k_y^2$ in Eqs. (26) and (28) to take into account the Fourier modes in both directions. However, the stability boundaries are the same as predicted by Eqs. (26) or (28).

To investigate the stability of front solutions (stripes) in a 2D medium, we add a perturbation to the front solution, $a_s(x)$, as follows:

$$a(x,y,t) = a_s(x) + \eta(x,t)e^{iky}. \tag{30}$$

Inserting Eq. (30) into Eq. (22), one obtains the following equation for $\eta(x,t)$:

$$\frac{\partial \eta(x,t)}{\partial t} = \{\alpha - 3\beta[a_s(x)]^2\}\eta(x,t) + \frac{\partial^2 \eta(x,t)}{\partial x^2} - k^2\eta(x,t) + \varepsilon e^{\frac{-\sigma^2 k^2}{2}} \int_{-\frac{L}{2}-x}^{\frac{L}{2}-x} \frac{\eta(x',t)}{N\sqrt{2\pi}\sigma} e^{-(x'-x)^2/2\sigma^2} dx'. \tag{31}$$

Once $a_s(x)$ is determined, we examine its stability by calculating the maximum Lyapunov exponent using the formula

$$\lambda = \lim_{t\to\infty} \frac{1}{t} \ln \frac{\|\eta(x,t)\|}{\|\eta(x,0)\|} \tag{32}$$

with $\eta(x,t)$ numerically solved using Eq. (31). For a given k, one can obtain a λ. By scanning k, one obtains the curve of λ versus k. Figure 9(a) shows λ versus k for different σ values for a single-stripe solution [see the pattern in the first column in Fig. 9(d)]. For both small and large σ, $\lambda < 0$ for any k, indicating that the stripe is stable in the 2D medium [also see the 2D examples ($\sigma = 10$ and 200) in Fig. 9(d)]. For intermediate σ, λ can be positive for certain k values, indicating that the stripe is unstable in the 2D medium [also see the 2D examples ($\sigma = 20$ and 50) in Fig. 9(d)]. Figure 9(c) shows $\eta(x,t)$ at four time points for the case of $\sigma = 50$ for which the stripe is unstable. $\eta(x,t)$ grows at the front regions but shrinks at other regions, indicating that the transverse instabilities occur at the front regions.

To investigate how the transverse instability is affected by the Gaussian-weighted feedback, we scan σ and ε to determine the stability boundary of the single-stripe front solution by calculating λ using Eq. (31) [Fig. 9(b)]. The stripe pattern is unstable in the colored region and labyrinths emerge. The upper boundary of the colored region is where transverse instability occurs. The lower boundary is where the single-stripe solution is unstable in the 1D medium (longitudinal instability, not the transverse instability as for the upper boundary). To confirm the theoretical predictions, we also carry out simulations of 2D media by adding a random perturbation to the single-stripe solution to examine the transverse instability [snapshots in Fig. 9(d) show the stabilities of the fronts for selected σ]. The blue circles in Fig. 9(b) mark the stability boundary determined by direct 2D simulations, which agree

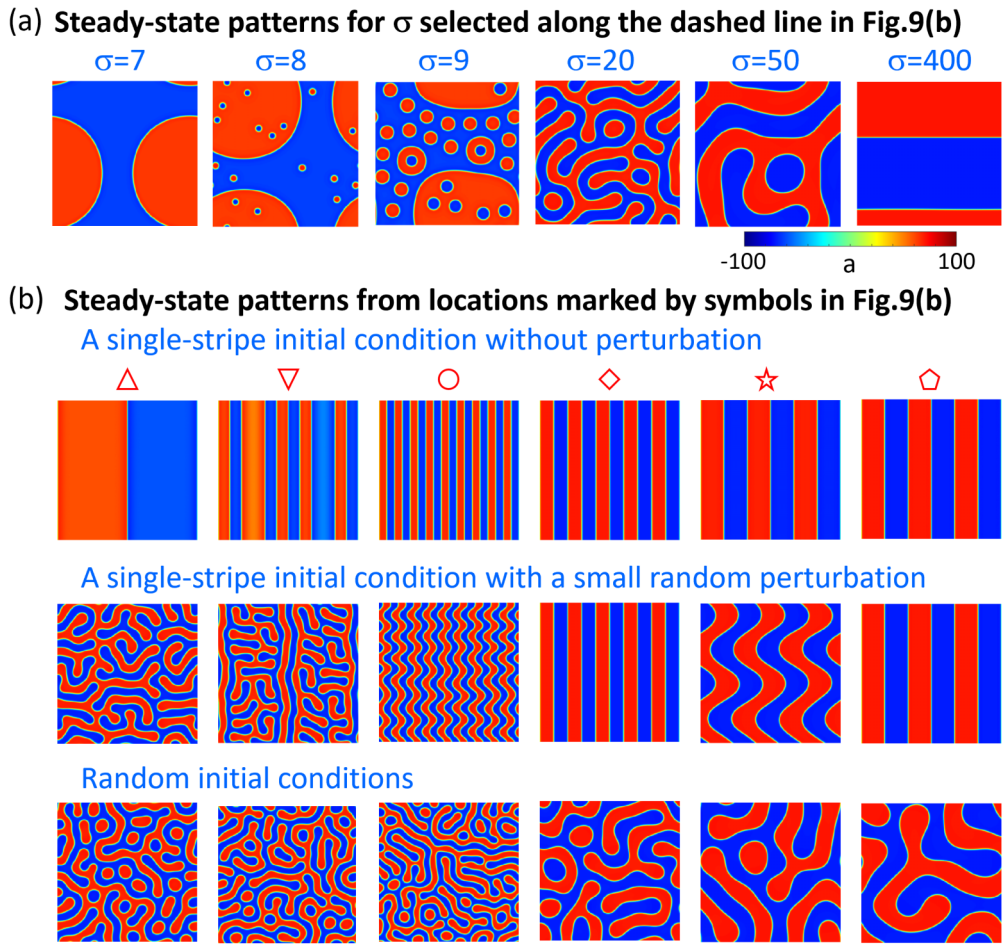


FIG. 10. Patterns in 2D media of the AE model with NUGF. (a) Steady-state patterns started from random initial conditions for selected σ values (marked) along the dashed line in Fig. 9(b). (b) Steady-state patterns from three different initial conditions for parameters selected from locations marked by the symbols in Fig. 9(b). Upper: steady-state patterns (taken at $t = 10\,000$) started from a single-stripe pattern (as the pattern in the first panel). Middle: same initial condition as for the upper panels but a small random perturbation is given at $t = 1000$. Bottom: steady-state patterns started from completely random initial conditions. The parameter sets (σ, ε) for the three cases are (from triangle to pentagon): (15, –0.15), (15, –0.25), (15, –0.45), (35, –0.45), (50, –0.45), and (60, –0.45).

accurately with the theoretical prediction using the Lyapunov exponent calculated from simulations of Eq. (31).

Using random initial conditions, we can observe different patterns depending on the parameters chosen. Figure 10(a) shows different patterns at different σ (the width of the Gaussian function) values along the dashed line in Fig. 9(b). When σ is very small, we observe single-circle or stripe patterns. This agrees with stability predicted in Fig. 9(b) that the front solution is stable when σ is small. As σ increases, we observe a new type of pattern: small circles superimposing on large stripes or circles. When σ is increased to the regime of lateral instability, labyrinths occur. When σ is sufficiently large, which is out of the regime of lateral instability, only single-circle or stripe patterns occur.

Below the colored region (or the blue curve), the single-stripe solution undergoes a longitudinal instability, leading to multistripe steady-state patterns if no random perturbations are given [the upper panels in Fig. 10(b)]. If a small random perturbation is given at some time point ($t = 1000$ in the simulations), it results in different patterns for different parameter locations [middle panels in Fig. 10(b)]: labyrinths, wavy stripes, and straight stripes (the same as those without perturbation). This indicates that the multistripe patterns are either transversely unstable or stable, depending on the parameter locations. However, when started with random initial conditions, the resulting steady-state patterns are all labyrinths [lower panels in Fig. 10(b)].

We carry out simulations of 2D media with the BZ model and the periodically paced FHN model in the presence of NUGF. In both models, we observe almost the same pattern behaviors as in the AE model. Here we only show some of the patterns observed in the BZ model (Figs. 11 and 12). In addition to stripes, circular clusters, and labyrinths, we also observe conducting waves and period-3 patterns when ε is large. Unlike the alternating patterns, the period-3 patterns are spatially random clusters [Fig. 11(c)]. Not surprisingly, we can demonstrate the lateral instability in the BZ reaction [Fig. 12(a)] the same way as in the AE model [Fig. 9(d)], i.e., the stripe pattern is unstable in a certain range of σ, which degenerates into labyrinths after a small perturbation. We also find other initial condition-dependent patterns in the BZ reaction as in the AE model. For example, in a set of ε and σ

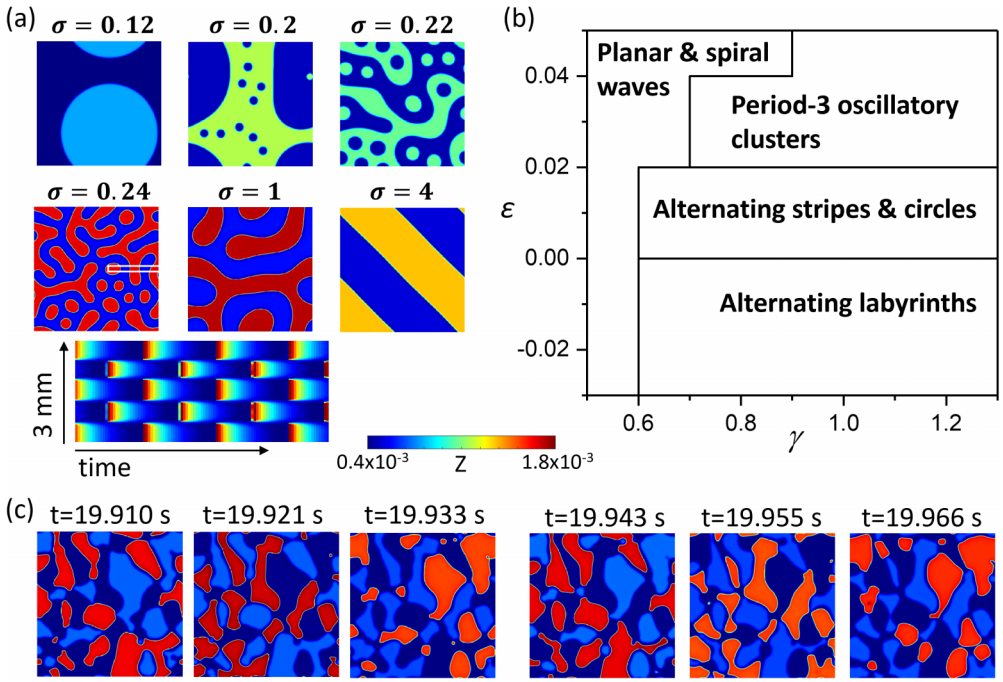


FIG. 11. Pattern formation in a 2D medium of the BZ reaction model with NUGF. (a) Snapshots of Z (see color bar) showing steady-state patterns with different σ values (unit: mm). $\gamma = 1$ and $\varepsilon = -0.01$. The snapshots are taken at the end of each simulation, not at the same phase of a period, and thus the colors are different for the panels. The line scan below the snapshots is taken from $\sigma = 0.24$ mm in a location marked by the open bar, showing the spatiotemporally alternating pattern. (b) Phase diagram showing pattern behaviors on γ-ε plane. (c) Snapshots showing patterns of period-3 oscillatory clusters. $\gamma = 1$, $\varepsilon = 0.03$, and $\sigma = 0.24$ mm. The snapshots are taken roughly at the same phase of the period but not exactly. The size of the medium is $L = 8$ mm.

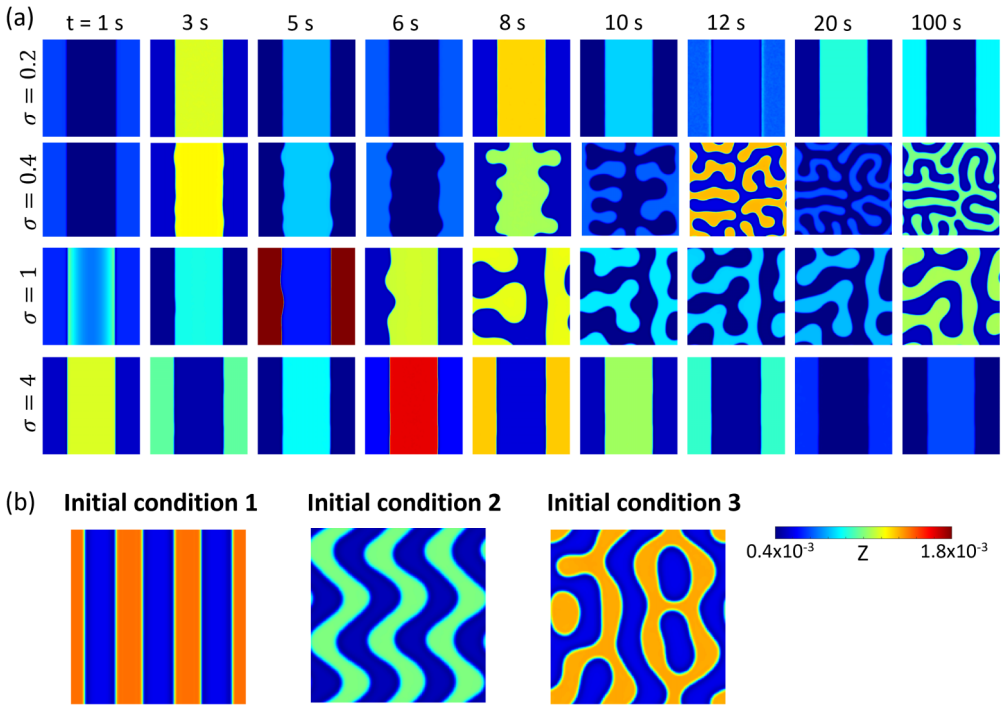


FIG. 12. Lateral instability in a 2D BZ reaction medium with NUGF. (a) Snapshots of Z (see color bar) in an 8 mm $\times$ 8 mm medium taken at different time points for different σ values (unit: mm) as marked. $\gamma = 1$ and $\varepsilon = -0.01$. The initial condition ($t = 0$) is a single-stripe front solution (pattern in the first column). A small random perturbation is given at $t = 1$ s. (b) Steady-state patterns (taken at $t = 100$ s) started from a single-stripe pattern [as the pattern in the first panel in (a)] without random perturbation (initial condition 1), a single-stripe pattern with a small random perturbation (initial condition 2), and a fully random initial condition (initial condition 3). $\gamma = 1$, $\varepsilon = -0.04$, and $\sigma = 0.42$ mm. The medium size is 4 mm $\times$ 4 mm.

[Fig. 12(b)], the single-stripe pattern is unstable, degenerating into multiple stripes if no random perturbation is given. If a small random perturbation is given, it degenerates into a wavy stripe pattern. If a pure random initial condition is given, the final pattern is a labyrinth pattern. These patterns are similar to the ones in the AE model shown in Fig. 10(b).

III. DISCUSSION AND CONCLUSIONS

In this study, we performed theoretical analyses and numerical simulations to investigate pattern formation in oscillatory media with UGF and NUGF. The theoretical predictions from the AE model are that under UGF, only alternating stripes and circles can be observed. Under NUGF, new patterns can form. In addition to alternating stripes and circles, one type of pattern is small alternating circles superimposing on alternating large circles or stripes. Another type of pattern is alternating labyrinths, which are caused by the front instability caused by NUGF. Other patterns, such as wavy stripes, are also observed. The theoretical predictions are validated using simulations of chemical reaction models and periodically paced excitable media, i.e., the periodically paced FHN model.

One major contribution of this study is the use of AE to perform stability analysis both analytically and numerically, which provides mechanistic insights into the formation and selection of the different alternating patterns, unifying the pattern dynamics observed in different chemical and biological systems under a single theoretical framework. The prediction that steady-state patterns under UGF are stripes and circular clusters, in particular, a single circular cluster as the most likely final pattern from a random initial condition implies that the noncircular cluster patterns observed in experiments [e.g., Fig. 1(b)] may still be transient patterns. However, the evolution to the final circular pattern is a very slow process (Figs. 6 and 7). The prediction that lateral instability leading to labyrinths occurs at the intermediate σ values of the Gaussian function implies that it requires some of the reactants in the feedback loop to exhibit certain diffusion rates since σ is a measure of the diffusion rate. More specifically, since the lateral instability is promoted by a negative feedback loop (negative ε values), it requires a certain diffusion rate of the inhibitor relative to that of the activator, similar to what is required for the Turing instability leading to steady-state Turing patterns.

A major limitation of the AE model is that they can only be used for describing period-2 dynamics, not for other spatiotemporal dynamics. Therefore, it cannot be used for investigating the transition among other spatiotemporal dynamics and the alternating patterns. For example, steady-state labyrinths and travelling and spiral waves in *in vitro E. coli* Min protein systems have been observed [51,52], and to investigate the transitions from these spatiotemporal dynamics to the alternating cluster dynamics, one needs to use the detailed biochemical reaction models describing the Min protein dynamics. The second limitation is that in many systems, there is no apparent global feedback loops as in the AE model or the ones implemented in the reaction-diffusion models. An equivalent process is a feedback loop with the involved reactants diffusing in space. How the Gaussian function used in this study can be representative for this process needs to be investigated using detailed biochemical reaction models. The third limitation is that the AE model is completely phenomenological, not derived from the reaction-diffusion systems as done by Echebaria and Karma for alternans dynamics during cardiac conduction [46], a direct quantitative comparison of the AE model with the reaction-diffusion models is not feasible. Future studies need to be done first to recapture the pattern dynamics observed in experiments using detailed reaction-diffusion models without the apparent global feedback loops and then validate the AE model both qualitatively and quantitatively. Nevertheless, our theoretical analyses provide a general mechanistic understanding of the formation of the alternating pattern dynamics in oscillatory media.

ACKNOWLEDGMENTS

This study was supported by NIH Grants No. R01 HL175074 and No. P01 HL164311 (Z.Q.) and by National Natural Science Foundation of China Grant No. 12505040 (C.H.).

DATA AVAILABILITY

There are no publicly available research data or software supporting this manuscript. Requests for further information or data should be sent to the authors.

APPENDIX: MATHEMATICAL MODELS AND NUMERICAL METHODS

Periodic boundary conditions are used for all models in the computer simulations. Simulations are done using graphic processing units with Nvidia CUDA programing.

1. Default parameters and numerical methods for the amplitude equations

The default parameters for the UGF case are $\alpha = 0.5$, $\beta = 0.0001$, and $\gamma = -0.012$. The default parameters for the NUGF case are $\alpha = 0.5$, $\beta = 0.0001$, $\gamma = 0$, and $\varepsilon = -0.1$. Parameters that are different from the default values are stated in the corresponding figure legends. The AE is discretized with $\Delta x = \Delta y = 1$ and $\Delta t = 0.01$ for numerical simulations.

2. Periodically paced FHN model with a delayed global feedback loop

The periodically paced FHN model is the same as one used in our previous study [44], i.e.,

$$\frac{\partial u}{\partial t} = f(u, v) + D\nabla^2 u + I(t), \tag{A1}$$

$$\frac{\partial v}{\partial t} = g(u, v), \tag{A2}$$

where $f(u, v) = -u(u-1)(u-0.5) - 0.1v$ and $g(u, v) = (u-0.25v-0.3)/10$. $I(t)$ is the stimulus, which also includes

the feedback terms as follows:

$$I(t) = \begin{cases} I_0[1 + \gamma(\bar{u}_{n-1} - \bar{u}_s) + \varepsilon(\bar{u}_{n-1,g} - \bar{u}_s)], & \text{if } nT < t < nT + \Delta T \\ 0, & \text{otherwise} \end{cases} \tag{A3}$$

In Eq. (A3), $\bar{u}_{n-1}$ is the spatial average at the peak of the $(n-1)$th beat and $\bar{u}_{n-1,g}$ is the Gaussian-weighted spatial average at the peak of the $(n-1)$th beat calculated the same way as Eq. (23) for 1D media and Eq. (24) for 2D media. Therefore, the time delay of the feedback is T. The parameters are $I_0 = 1.2$, $\bar{u}_s = 0.77$, $T = 45$, $\Delta T = 0.5$, and $D = 0.1$. We use $\gamma = -0.3$ and $\varepsilon = 0$ for UGF and $\gamma = 0$ and $\varepsilon = -0.1$ for NUGF. The differential equations are discretized with $\Delta x = \Delta y = 1$ and $\Delta t = 0.01$ for numerical simulations.

3. BZ reaction model with a global feedback loop

The BZ reaction model with a UGF loop was used previously to simulate alternating stripes [12,41]. Here we add to this model a NUGF loop with the feedback strength described by a Gaussian-weighted spatial average of one of the reactants. The partial differential equations of the modified BZ reaction are

$$\frac{\partial X}{\partial t} = \frac{-k_2 X + k_3 A}{k_2 X + k_3 A}\left[\frac{q k_7 k_8 BZ}{k_8 + k_{-7} h_0 (C - Z)} + k_9 B + \gamma(\bar{Z} - Z_t) + \varepsilon(\bar{Z}_g - Z_t)\right] - 2k_4 X^2 + k_5 h_0 AX - k_{-5} U^2 + D_X \nabla^2 X, \tag{A4}$$

$$\frac{\partial Z}{\partial t} = k_6 U(C - Z) - k_{-6} XZ - \frac{k_7 k_8 BZ}{k_8 + k_{-7} h_0 (C - Z)} + D_Z \nabla^2 Z, \tag{A5}$$

where X and Z are the reactants and U is a function of X and Z, i.e., $U = \frac{-k_6(C-Z) + \sqrt{[k_6(C-Z)]^2 + 8k_{-5}(2k_5 h_0 AX + k_{-6} XZ)}}{4k_{-5}}$. $\gamma(\bar{Z} - Z_t)$ is the UGF term, with $\bar{Z}$ being the spatial average of Z and $Z_t = 0.0005$. $\varepsilon(\bar{Z}_g - Z_t)$ is the NUGF term with $\bar{Z}_g$ a Gaussian-weighted spatial average of Z calculated the same way as Eq. (23) for 1D media and Eq. (24) for 2D media. The parameters are the same as in Refs. [12,41]. In numerical simulations, the differential equations are discretized with $\Delta x = \Delta y = 0.02$ mm and $\Delta t = 0.001$ s.

4. CO oxidation on Pt(110) model with a delayed global feedback loop

The CO oxidation on the Pt(110) model is the same as that in Ref. [14] with the following differential equations:

$$\frac{\partial u}{\partial t} = k_1 S_{\mathrm{CO}} P_{\mathrm{CO}}(1 - u^3) - k_2 u - k_3 uv + D\nabla^2 u, \tag{A6}$$

$$\frac{dv}{dt} = k_4 P_{O_2}[S_{O,1\times1} w + S_{O,1\times2}(1 - w)](1 - u - v)^2 - k_3 uv, \tag{A7}$$

$$\frac{dw}{dt} = k_5\left[1 + \exp\left(\frac{u_0 - u}{\delta}\right)\right]^{-1} - k_5 w. \tag{A8}$$

The global delayed feedback is introduced by setting $P_{\mathrm{CO}}(t) = p_0 - \mu[\bar{u}(t-\tau) - u_{\mathrm{ref}}]$, where τ is the time delay and $\bar{u}(t-\tau)$ is the spatial average calculated at $t' = (t-\tau)$. All parameters are the same as in Ref. [14]. The differential equations are discretized with $\Delta x = \Delta y = 4$ and $\Delta t = 0.001$ for computer simulations. Due to computational limitations, we only simulated the UGF case for this model since for the NUGF case, one needs to store the information for every spatial and time points for a time period of τ to calculate the Gaussian function, which is beyond our current computational capability.

[1] P. Ball, *The Self-Made Tapestry: Pattern Formation in Nature* (Oxford University Press, Oxford, 1999).

[2] M. Cross and H. Greenside, *Pattern Formation and Dynamics in Nonequilibrium Systems* (Cambridge University Press, Cambridge, 2009).

[3] A. M. Turing, The chemical basis of morphogenesis, Philos. R. Soc. London B **237**, 37 (1952).

[4] Q. Ouyang and H. L. Swinney, Transition from a uniform state to hexagonal and striped Turing patterns, Nature (London) **352**, 610 (1991).

[5] S. Kondo and T. Miura, Reaction-diffusion model as a framework for understanding biological pattern formation, Science **329**, 1616 (2010).

[6] P. K. Maini, R. E. Baker, and C. M. Chuong, The Turing model comes of molecular age, Science **314**, 1397 (2006).

[7] V. K. Vanag and I. R. Epstein, Pattern formation mechanisms in reaction-diffusion systems, Int. J. Dev. Biol. **53**, 673 (2009).

[8] V. K. Vanag and I. R. Epstein, Pattern formation in a tunable medium: The Belousov-Zhabotinsky reaction in an aerosol OT microemulsion, Phys. Rev. Lett. **87**, 228301 (2001).

[9] L. Yang and I. R. Epstein, Oscillatory turing patterns in reaction-diffusion systems with two coupled layers, Phys. Rev. Lett. **90**, 178303 (2003).

[10] L. Yang, A. M. Zhabotinsky, and I. R. Epstein, Stable squares and other oscillatory turing patterns in a reaction-diffusion model, Phys. Rev. Lett. **92**, 198303 (2004).

[11] V. K. Vanag and I. R. Epstein, Stationary and oscillatory localized patterns, and subcritical bifurcations, Phys. Rev. Lett. **92**, 128301 (2004).

[12] V. K. Vanag, L. Yang, M. Dolnik, A. M. Zhabotinsky, and I. R. Epstein, Oscillatory cluster patterns in a homogeneous chemical system with global feedback, Nature (London) **406**, 389 (2000).

[13] V. K. Vanag, A. M. Zhabotinsky, and I. R. Epstein, pattern formation in the Belousov−Zhabotinsky reaction with photochemical global feedback, J. Phys. Chem. A **104**, 11566 (2000).

[14] M. Kim, M. Bertram, M. Pollmann, A. v. Oertzen, A. S. Mikhailov, H. H. Rotermund, and G. Ertl, Controlling chemical turbulence by global delayed feedback: Pattern formation in catalytic CO oxidation on Pt(110), Science **292**, 1357 (2001).

[15] V. Petrov, Q. Ouyang, and H. L. Swinney, Resonant pattern formation in a chemical system, Nature (London) **388**, 655 (1997).

[16] A. L. Lin, M. Bertram, K. Martinez, H. L. Swinney, A. Ardelea, and G. F. Carey, Resonant phase patterns in a reaction-diffusion system, Phys. Rev. Lett. **84**, 4240 (2000).

[17] S. Kretschmer, T. Heermann, A. Tassinari, P. Glock, and P. Schwille, Increasing MinD's membrane affinity yields standing wave oscillations and functional gradients on flat membranes, ACS Synth. Biol. **10**, 939 (2021).

[18] A. Kaminaga, V. K. Vanag, and I. R. Epstein, Wavelength halving in a transition between standing waves and traveling waves, Phys. Rev. Lett. **95**, 058302 (2005).

[19] Z. Qu and J. N. Weiss, Cardiac alternans: From bedside to bench and back, Circ. Res. **132**, 127 (2023).

[20] J. Kockskamper and L. A. Blatter, Subcellular Ca^{2+} alternans represents a novel mechanism for the generation of arrhythmogenic Ca^{2+} waves in cat atrial myocytes, J. Physiol. **545**, 65 (2002).

[21] M. E. Diaz, D. A. Eisner, and S. C. O'Neill, Depressed ryanodine receptor activity increases variability and duration of the systolic Ca^{2+} transient in rat ventricular myocytes, Circ. Res. **91**, 585 (2002).

[22] S. A. Gaeta, G. Bub, G. W. Abbott, and D. J. Christini, Dynamical mechanism for subcellular alternans in cardiac myocytes, Circ. Res. **105**, 335 (2009).

[23] G. L. Aistrup, Y. Shiferaw, S. Kapur, A. H. Kadish, and J. A. Wasserstrom, Mechanisms underlying the formation and dynamics of subcellular calcium alternans in the intact rat heart, Circ. Res. **104**, 639 (2009).

[24] L. H. Xie and J. N. Weiss, Arrhythmogenic consequences of intracellular calcium waves, Am. J. Physiol. Heart Circ. Physiol. **297**, H997 (2009).

[25] D. S. Rosenbaum, L. E. Jackson, J. M. Smith, H. Garan, J. N. Ruskin, and R. J. Cohen, Electrical alternans and vulnerability to ventricular arrhythmias, N. Engl. J. Med. **330**, 235 (1994).

[26] J. N. Weiss, A. Karma, Y. Shiferaw, P. S. Chen, A. Garfinkel, and Z. Qu, From pulsus to pulseless: The saga of cardiac alternans, Circ. Res. **98**, 1244 (2006).

[27] D. M. Raskin and P. A. J. de Boer, Rapid pole-to-pole oscillation of a protein required for directing division to the middle of *Escherichia coli*, Proc. Natl. Acad. Sci. USA **96**, 4971 (1999).

[28] X. Fu, Y.-L. Shih, Y. Zhang, and L. I. Rothfield, The MinE ring required for proper placement of the division site is a mobile structure that changes its cellular location during the *Escherichia coli* division cycle, Proc. Natl. Acad. Sci. USA **98**, 980 (2001).

[29] C. A. Hale, H. Meinhardt, and P. A. J. de Boer, Dynamic localization cycle of the cell division regulator MinE in Escherichia coli, EMBO J. **20**, 1563 (2001).

[30] R. A. Kerr, H. Levine, T. J. Sejnowski, and W.-J. Rappel, Division accuracy in a stochastic model of Min oscillations in *Escherichia coli*, Proc. Natl. Acad. Sci. USA **103**, 347 (2006).

[31] A. Amiranashvili, N. D. Schnellbächer, and U. S. Schwarz, Stochastic switching between multistable oscillation patterns of the Min-system, New J. Phys. **18**, 093049 (2016).

[32] D. Fange and J. Elf, Noise-induced Min phenotypes in *E. coli*, PLoS Comput. Biol. **2**, e80 (2006).

[33] H. Meinhardt and P. A. J. de Boer, Pattern formation in Escherichia coli: A model for the pole-to-pole oscillations of Min proteins and the localization of the division site, Proc. Natl. Acad. Sci. USA **98**, 14202 (2001).

[34] K. Zieske and P. Schwille, in *Methods in Cell Biology*, edited by J. Ross and W. F. Marshall, (Academic, 2015), Vol. 128, p. 149.

[35] M. Bonny, E. Fischer-Friedrich, M. Loose, P. Schwille, and K. Kruse, Membrane binding of MinE allows for a comprehensive description of min-protein pattern formation, PLoS Comput. Biol. **9**, e1003347 (2013).

[36] L. Wettmann and K. Kruse, The Min-protein oscillations in *Escherichia coli*: An example of self-organized cellular protein waves, Philos. Trans. R. Soc. London B Biol. Sci. **373**, 20170111 (2018).

[37] Z. Ren, H. Weyer, M. Sandler, *et al.*, Robust and resource-optimal dynamic pattern formation of Min proteins *in vivo*, Nat. Phys. **21**, 1160 (2025).

[38] K. Zieske and P. Schwille, Reconstitution of self-organizing protein gradients as spatial cues in cell-free systems, eLife **3**, e03949 (2014).

[39] M. Falcke and H. Engel, Pattern formation during the CO oxidation on Pt(110) surfaces under global coupling, J. Chem. Phys. **101**, 6255 (1994).

[40] M. Falcke, H. Engel, and M. Neufeld, Cluster formation, standing waves, and stripe patterns in oscillatory active media with local and global coupling, Phys. Rev. E **52**, 763 (1995).

[41] L. Yang, M. Dolnik, A. M. Zhabotinsky, and I. R. Epstein, Oscillatory clusters in a model of the photosensitive Belousov-Zhabotinsky reaction system with global feedback, Phys. Rev. E **62**, 6414 (2000).

[42] M. Bertram and A. S. Mikhailov, Pattern formation in a surface chemical reaction with global delayed feedback, Phys. Rev. E **63**, 066102 (2001).

[43] Y. Shiferaw and A. Karma, Turing instability mediated by voltage and calcium diffusion in paced cardiac cells, Proc. Natl. Acad. Sci. USA **103**, 5670 (2006).

[44] Z. Song and Z. Qu, Delayed global feedback in the genesis and stability of spatiotemporal excitation patterns in paced biological excitable media, PLoS Comput. Biol. **16**, e1007931 (2020).

[45] C. Huang, Z. Song, and Z. Qu, Transition from alternating stripes to alternating labyrinths in oscillatory media, Phys. Rev. E **111**, L032201 (2025).

[46] B. Echebarria and A. Karma, Instability and spatiotemporal dynamics of alternans in paced cardiac tissue, Phys. Rev. Lett. **88**, 208101 (2002).

[47] B. Echebarria and A. Karma, Amplitude equation approach to spatiotemporal dynamics of cardiac alternans, Phys. Rev. E **76**, 051911 (2007).

[48] C. Huang, Z. Song, Z. Di, and Z. Qu, Stability of spatially discordant repolarization alternans in cardiac tissue, Chaos **30**, 123141 (2020).

[49] C. Huang, Z. Song, and Z. Qu, Synchronization of spatially discordant voltage and calcium alternans in cardiac tissue, Phys. Rev. E **106**, 024406 (2022).

[50] J. P. Keener and J. Sneyd, *Mathematical Physiology* (Springer, New York, 1998).

[51] M. Loose, E. Fischer-Friedrich, J. Ries, K. Kruse, and P. Schwille, Spatial regulators for bacterial cell division self-organize into surface waves in vitro, Science **320**, 789 (2008).

[52] B. Ramm, A. Goychuk, A. Khmelinskaia, P. Blumhardt, H. Eto, K. A. Ganzinger, E. Frey, and P. Schwille, A diffusiophoretic mechanism for ATP-driven transport without motor proteins, Nat. Phys. **17**, 850 (2021).